

Statistical segmentation and porosity quantification of 3D X-ray micro-tomography

Daniela Ushizima^a, Dilworth Parkinson^b, Peter Nico^c, Jonathan Ajo-Franklin^c,
Alastair Macdowell^b, Benjamin Kocar^d, Wes Bethel^a and James Sethian^e

^aComputational Research Division, Lawrence Berkeley National Laboratory, Berkeley CA 94720, USA;

^bAdvanced Light Source Division, Lawrence Berkeley National Laboratory, Berkeley CA 94720, USA;

^cEarth Science Division, Lawrence Berkeley National Laboratory, Berkeley CA 94720, USA;

^dDepartment of Environmental Systems Science, Stanford University, Stanford CA 94305;

^eMath Department, University of California, Berkeley CA 94720, USA.

ABSTRACT

High-resolution x-ray micro-tomography is used for imaging of solid materials at micrometer scale in 3D. Our goal is to implement nondestructive techniques to quantify properties in the interior of solid objects, including information on their 3D geometries, which supports modeling of the fluid dynamics into the pore space of the host object. The micro-tomography data acquisition process generates large data sets that are often difficult to handle with adequate performance when using current standard computing and image processing algorithms. We propose an efficient set of algorithms to filter, segment and extract features from stacks of image slices of porous media. The first step tunes scale parameters to the filtering algorithm, then it reduces artifacts using a fast anisotropic filter applied to the image stack, which smoothes homogeneous regions while preserving borders. Next, the volume is partitioned using statistical region merging, exploiting the intensity similarities of each segment. Finally, we calculate the porosity of the material based on the solid-void ratio. Our contribution is to design a pipeline tailored to deal with large data-files, including a scheme for the user to input image patches for tuning parameters to the datasets. We illustrate our methodology using more than 2,000 micro-tomography image slices from 4 different porous materials, acquired using high-resolution X-ray. Also, we compare our results with standard, yet fast algorithms often used for image segmentation, which includes median filtering and thresholding.

Keywords: segmentation, porosity, visualization, x-ray tomography, carbon sequestration.

1. INTRODUCTION

Industrial processes as well as experimental setups of composites often require the description of materials in terms of their 3D architecture,²² the interactions between structures, etc. Three-dimensional synchrotron X-ray micro-tomography images permit non-destructive observation at different scales, virtual sectioning of the volume without damaging the original solid sample, and characterization of the media by means of parameters such as porosity and channel connectivity.

High resolution 3D micro-tomography image stacks can easily result in data files larger than 8 gigabytes. A common approach is to evaluate cropped samples of the original image stacks and/or work with a much lower resolution version of the data, defeating the purpose of the technology. This is a critical issue for the micro-tomography community as a whole who often have difficulties analyzing the collected data. In some cases, the challenge is just visualization of such large datasets, but in most cases, the harder task is to provide image segmentation and material characterization.

In collaboration with the Energy Frontier Research Center (EFRC) and Advanced Light Source (ALS), we have developed tools for micro-tomography image analysis and visualization, particularly designed to deal with porous media with applications to safe storage of CO₂ in deep subsurface rock formations: the goal is

Further author information: D.M.U.: E-mail: dushizima@lbl.gov, Telephone: 1 510 486 4061

This is a reviewed version from article submitted to:

SPIE Optics and Photonics 2011, Applications of Digital Image Processing XXXIV, Vol.8135-1 p.1-14

quantification of internal properties of imaged objects, including information about porosity. One of our tools is a framework that controls spurious heterogeneity of the images and identifies two phases in non-uniform composed materials: solid and pore space. This paper introduces this framework, designed to deal with image stacks of porous material. The main processing steps consist of noise reduction using 3D bilateral filtering, followed by segmentation between solid phase and void (or pore) space using 3D statistical region merging and porosity calculation.

Our motivation to use bilateral filtering comes from successful results in minimizing image artifacts with border preservation, in different imaging modalities, ranging from computed tomographic images,³⁵ diffusion tensor magnetic resonance imaging,¹⁷ video,²⁹ among others. We use the implementation proposed by Tomasi and Maducci³² and compare results with the 3D median filter¹⁸ since both of them are nonlinear filters.

Heide et al¹⁸ conducted detailed evaluation of filtering methods, and noticed that the first three iterations of the 3D median filter (a.k.a. *med3*) provide the largest gain in noise reduction of electron tomographic reconstructions. This investigation concluded that the *med3* outperformed others filters such as wavelet-based, adaptive Wiener and bilateral. We will show that using bilateral filtering can be more advantageous when applied to X-ray micro tomography of porous media, and also for synthetic images under low-to-medium levels of Gaussian noise.

In order to evaluate the segmentation methods, we compare results obtained using thresholding and statistical region merging in the detection of pore space. Thresholding algorithms¹⁶ are simple, fast and still largely used in computed tomography image segmentation, both in its more traditional version¹⁴ and more sophisticated implementations such as those using indicator kriging.^{27,30}

We discuss the advantages and limitations of each algorithmic approach, both in terms of qualitative illustrations and quantitative measurements of different material specimens. Our comparisons consider both synthetic and micro computed tomography (micro-CT) data, including performance evaluation in terms of accuracy gain when considering standard algorithms as the iterative median filtering and thresholding in comparison with bilateral filtering and statistical region merging.

First, we measure the amount of noise in order to have an indicator of image quality: this is done by using the coefficient of variance (CV), that provides parameters for image smoothing and border enhancement of micro-CT images automatically as in Sec.2.1-2.2. Second, we apply bilateral filtering for non-iterative anisotropic smoothing for minimizing noise and other artifacts as in Sec.2.1. Third, the statistical region merging algorithm calculates regions of interest, which outputs an over-segmented representation of the material. Then, we propose an algorithm for determining cut-offs to classify the data into material and pore space - this segmentation scheme is topic of Sec.2.3. Sec.3.3 discusses the results of feature extraction and illustrates the segmentation method using volume rendering. This pipeline lays the basis for further investigations related to material structure, porosity quantification and topological characterization of channels, discussed in future developments.

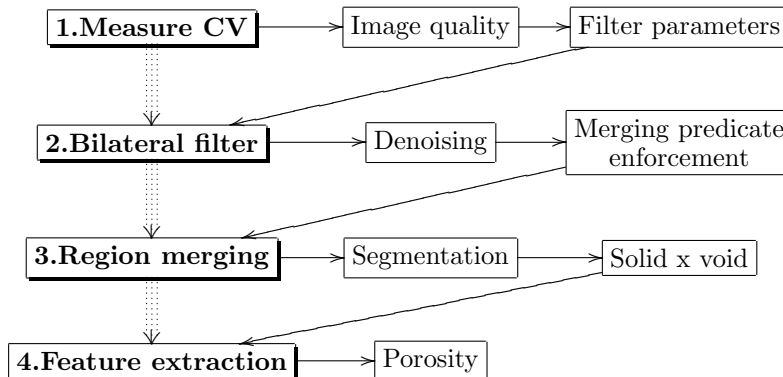


Figure 1: Pipeline for high-resolution x-ray micro-tomography image segmentation into two different phases for characterization of porosity.

2. MATERIALS AND METHODS

Our research relies on image analysis from composite preparation by personnel at the Energy Frontier Research Center(EFRC)² for Nanoscale Control of Geologic CO₂ and image acquisition at the Advanced Light Source (ALS),¹ beamline 8.3.2, both at Lawrence Berkeley National Laboratory. The ALS is a synchrotron, i.e. a specialized particle accelerator that generates bright beams of x-rays. The x-ray light directed down the beamlines is the result of electron bunches traveling near the speed of light, forced into a circular path by magnets. The image acquisition setup at the beamline can affect the image spatial representation by means of the size of each detector element, the magnification, the size of the focal spot, the geometric calibration of the rotating system and the reconstruction algorithm.⁹ Image artifacts, including streaking, makes segmentation challenging. The most significant cause of ring-artifacts, or streaks, are defects in or dirt on the scintillator, the device that converts the X-rays into visible light, which is ultimately captured by the CCD. A possible way of smoothing these spurious local variations, minimizing artifacts while preserving edge, is to use bilateral filtering.

High-resolution synchrotron-based X-ray spectromicroscopy is a nondestructive technique to visualize the interior of solid objects, enabling characterization of 3D geometries from volume data. The image database consists of CT scans known as micro-tomographic (microCT) images. These are the result of mapping the linear absorption coefficients of the sample into a filtered back-projection set, containing cross-sections of the object.²² The process of imaging the whole material sample involves acquiring projection views at several equally spaced angular positions around the sample. Each voxel conveys information about the X-ray attenuation and density of the scanned material as a gray level value.³⁰ Some of the advantages of microCT images are: (a) isotropy and pixel resolution at micrometer scale; (b) the possibility of creating 3D virtual models that are useful to the carbon sequestration research using synchrotron light radiation to probe the structure of porous materials.

We describe microCT samples acquired at beamline with energies between 10 and 45keV, with a 1% bandpass, CCD camera Cooke PCO 4000, Kodak chip with 4008 x 2672 pixels, 14 bit, 9 micron square pixels. The samples are pre-processed using a separate software¹³ that provides reconstruction of the parallel beam projection data into stacks of image slices, as illustrated at left of Fig.5-8. Different parametrization of reconstruction algorithms may result in different images with different levels of artifact corruption. Although image reconstruction is an important step in data acquisition, it is out of the scope of this paper. Further references may be found in.¹⁹⁻²¹

Our work focuses on the segmentation of the pore space, usually represented by lower gray level values, and it encloses four geologic samples of porous medium, composed by solid(s) (e.g. rock and other mineral sediments) and void (pore) space. The illustrations and descriptions of the datasets are as follows:

Table 1: Micro-CT stacks of images.

Figure	experiment	dimensions (WxHxD)	resolution (μm)	total (GB)
5	large sediments	1813 x 1813 x 501	1.7	3
6	glass beads	3337 x 3337 x 483	4.49	10
7	small sediments	1350 x 1350 x 1000	0.89	3.4
8	several sediments	2048 x 2048 x 400	1.69	3.2

Fig.5 shows a tube of large sediment grains, used in modeling experimental systems. These grains are laboratory synthesized and consist of iron oxide coated quartz sand. The contrast between solid and pore space is visually different when observing each slice individually. The aim is to segment pore space from grains, overcoming the ring-artifacts.

Fig.6 illustrates calcite precipitation induced in a glass bead-packed column in biogenic mixture, using the microbe *S. pasteurii*. Calcite is a mineral phase that can precipitate during subsurface remediation or geotechnical engineering processes, with possible behavior variations of the system, e.g. flow alternation and soil strengthening. More details about this geophysical research are in.^{7, 24}

Fig.7 shows a column of small sediment grains, also laboratory synthesized iron oxide coated quartz sand. Both Fig.7 and Fig.5 preparations are used in laboratory bio-remediation column experiments. The low contrast and reconstruction artifacts present in the images makes this segmentation challenging. The aim is to segment pore space from grains, which with largely heterogeneous granularity.

Fig.8 presents a shale sample, a sedimentary fine-grained rock, here with 4 different phases. Clay is the major constituent of these rocks, assuming dark gray intensity levels in this picture. The Illite phase is observed from tomography data as medium to light gray regions, while other phases such as pore and pyrite are observed as very dark and very bright intensity, respectively. The mid-gray shades are very challenging to identify. Illite, in particular, tends to occur as a very thin flake, sheet-like structure in the sample. Difficulties in multi-phase segmentation occur mostly around the bright pyrite region which ends up with a halo of illite when using standard thresholding algorithms for segmentation, which does not correspond to the real material composition. In this paper, we perform segmentation between pore and other materials.

In order to analyze these micro-CT images from diverse geological samples, we developed a single integrated pipeline (Fig.1) after we evaluate different algorithms, using synthetic and real manually segmented images, as described in the following sections.

2.1 Artifacts removal

MicroCT reconstructed images are often subjected to blur and noise due to light absorption/scattering, positioning of the samples, image reconstruction algorithms, among other factors. According to Buades et al,¹¹ the finite nature of images results in blurring while the number of photons and heating result in noise. In general terms, our paper refers to noise as any spurious artifacts that corrupt the original (ideal) image of the porous media.

The different samples illustrated in Fig.5-8 were acquired using the same device, different magnifications, and share common characteristics, such as the circular patterns following ring-like scattering. A possible way of smoothing the local variations, minimizing ring artifacts while preserving edges, is to use bilateral filtering, among other approaches.^{10,37}

Proposed by Tomasi and Manduchi,³² bilateral filtering combines geometric closeness (domain) and photometric similarity (range) to recalculate a pixel value. This algorithm is an attractive alternative to iterative diffusion methods due to its efficiency, particularly when dealing with large images.¹⁷ Further advances toward acceleration techniques for performance improvement of bilateral filtering can be found in.^{8,28,29,36}

The algorithm input is a noise-corrupted image $f(x)$ at position x , the filtered image $h(x)$ is the result of combining domain and range filtering according the following equations:

$$h(x) = k^{-1}(x) \int_{-\infty}^{\infty} \int_{-\infty}^{\infty} f(\xi) c(\xi, x) s(f(\xi), f(x)) d\xi \quad (1)$$

where $c(\xi, x)$ translates into distance between the center x and one of its neighbors ξ and $s(f(\xi), f(x))$ is proportional to the photometric similarity between $f(x)$ and $f(\xi)$. The normalization component, $k(x)$, guarantees that the weights for all the pixels add up to one.

$$k(x) = \int_{-\infty}^{\infty} \int_{-\infty}^{\infty} c(\xi, x) s(f(\xi), f(x)) d\xi \quad (2)$$

This locally adaptive filter computes a weighted average of the local neighborhood, where the weights are based on spatial and radiometric distances between the center and the neighboring samples. We used the implementation where both $c(\xi, x)$ and $s(f(\xi), f(x))$ are Gaussian functions, as originally described in³² and Fig.6 exemplifies the ability of removing artifacts from micro-CT by applying such a filter.

Figure 3 illustrates the results of using different parameters. As expected, σ_r has less effect for smaller values of σ_d and the range filter preserves more edges for smaller values of σ_r . The combination of higher values for both parameters can deteriorate borders of the volume of interest, as illustrated by the small sediments on the top of Figure 3(f).

We noticed that the inclusion of a frequency distribution of the gray values in the calculation of the new pixel has proven to mitigate the ring artifacts by compressing the histogram to a narrower vicinity. This gray level remapping supports the next processing step, the statistical region growing, by restricting the variation according

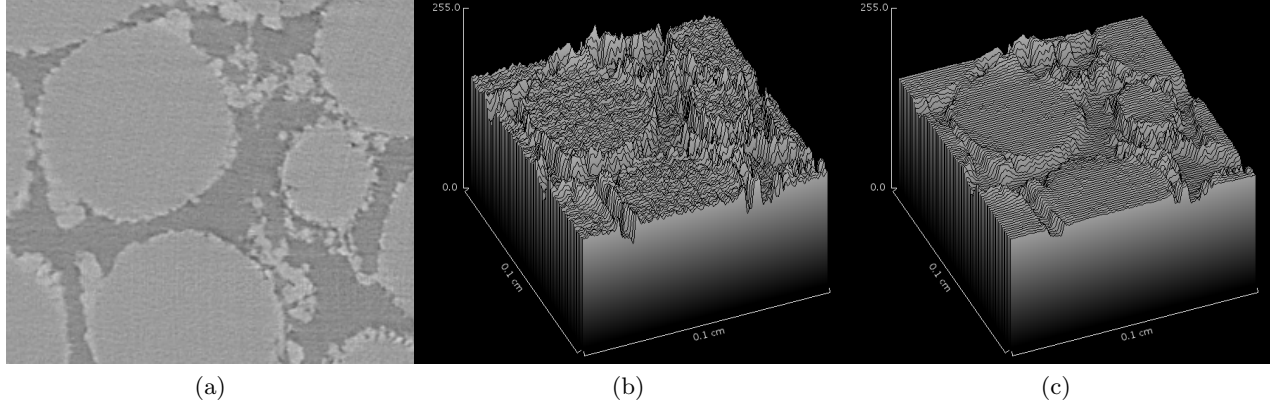


Figure 2: Removing artifacts from micro-CT slices: (a) slice of Fig.6, (b) topographical representation of (a) and (c) filtered result.

to distance while preserving the borders of the rocks and small sediments. The Gaussian kernels attenuate the influence of pixels in the vicinity of a target pixel, and they depend on geometrical closeness (σ_d) and pixel depth (σ_r) difference. Then, we need to find a good way to estimate these parameters, which is the topic of the next section.

2.2 Estimating filtering parameters

Filter parametrization can undermine the designing of a framework targeted to be generic enough for denoising different image datasets. We circumvent this problem by proposing an algorithm that turns user-input image patches into suitable parameters to the bilateral filter. More specifically, we estimate parameter σ_r , used in the calculation of the radiometric distances between the center and the neighboring samples for bilateral filtering.

The core idea here is to have a calibration phase, by when the user interactively crops image patches as representative subvolumes of the foreground and background. Each patch consists of the current slice and the two immediately adjacent ones. Next, the algorithm computes the quotient of the standard deviation (σ) and the average signal in a region of interest, also known as the coefficient of variation (CV) defined as $CV = \frac{\sigma}{|\mu|}$. The algorithm compares different patches in terms of their degree of gray level variations using CV. This step is essential because the averages of the image patches can be widely different from each other, even if they belong to the same region of interest (e.g. foreground) - CV analysis allows patch comparisons despite the presence of spatial variations regarding image noise and brightness. Finally, the proposed algorithm considers the gray level statistics of the patch P with the largest CV to determine σ_r by calculating the following steps:

FILTER-TUNING(P)

```

1   $h \leftarrow hist(P)$ ;  $\mu \leftarrow mean(P)$ ;  $\sigma \leftarrow std(P)$ ;
2   $\alpha \leftarrow round(\mu - \sigma)$ ;  $\beta \leftarrow round(\mu + \sigma)$ ;
3  repeat
4       $\gamma = \sum_{i=\alpha}^{\beta} h(i)$ 
5      if  $\gamma \geq (0.95 * |P|)$ 
6          then return
7      else  $\alpha \leftarrow \alpha - 1$ ;  $\beta \leftarrow \beta + 1$ ;
8  until  $(\alpha > 0)$  and  $(\beta < 255)$ 
9   $\sigma_r = \beta - \alpha$ 
10 return  $(\sigma_r)$ 
```

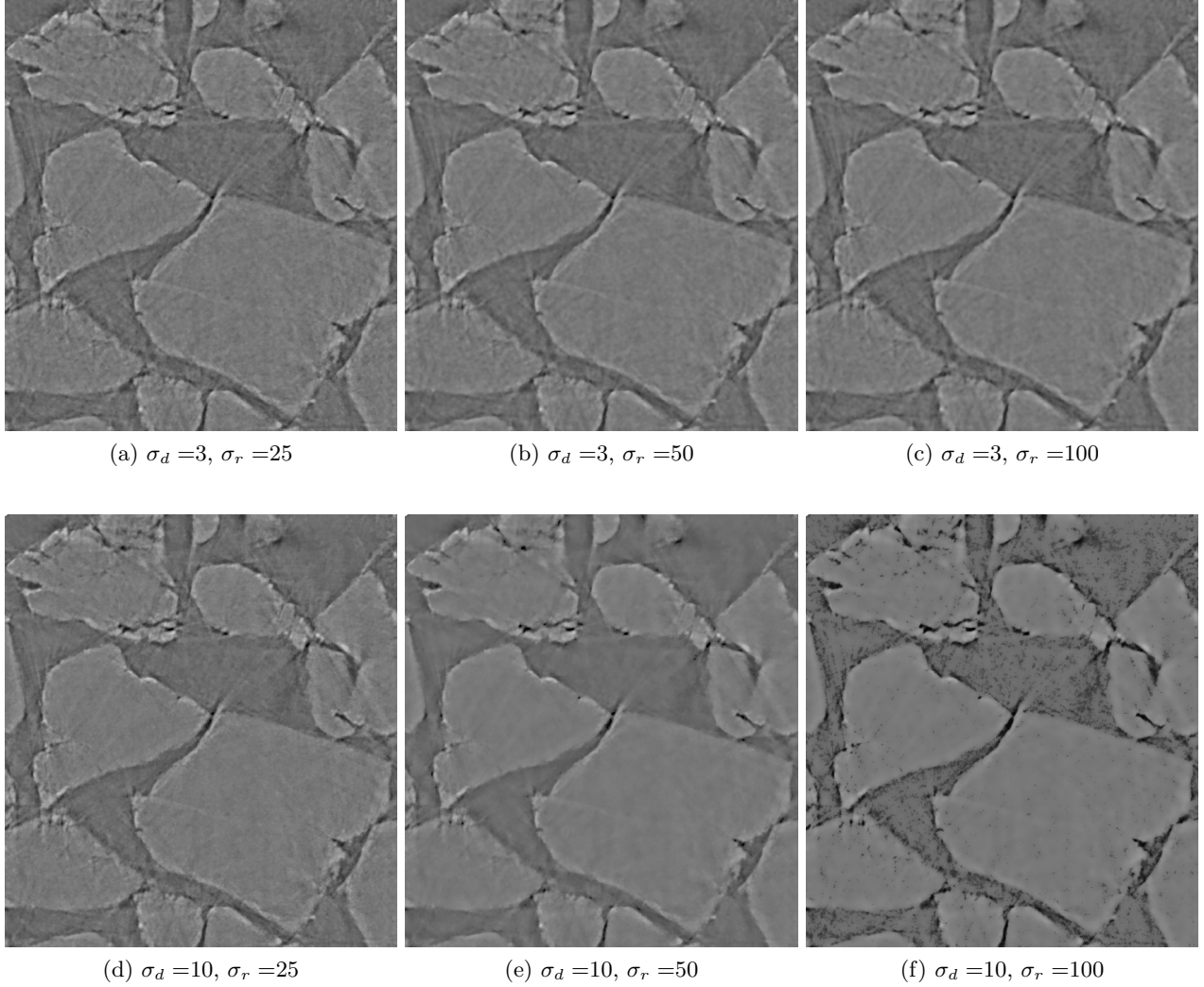


Figure 3: Detail of image slice of iron-sand composite to illustrate artifact removal: row parameter is $\sigma_d = [3, 10]$ and column is $\sigma_r = [25, 50, 100]$

The percentage of pixels (95%) corresponds to 4σ approximately, if the distribution follows a normal curve. The proposed approach outputs a range parameter from user-selected patches of micro-CT. This relies on the assumption that the largest variation among selected patches encloses sufficient statistics to represent the range of voxel intensity levels encompassed by the background or foreground in a image stack. This parameter allows suitable filtering, decreases artifacts as fringes and other spurious variations, and improves the results of the adopted segmentation algorithm, discussed in the next section.

2.3 Statistical Region Merging

One of the most challenging steps in image understanding is the segmentation of the region of interest, whose solution often depends on the targeting scale. This idea illustrates the concept of hierarchical segmentation, a class of algorithms that includes region merging techniques. Statistical region merging (SRM) is a region growing segmentation algorithm based on an adaptive statistical threshold merging predicate on intensity levels. Particular advantages of using this algorithm for dealing with large images are that it dispenses dynamical maintenance of a region adjacency graph (RAG), allows defining a hierarchy of partitions and it runs in linear-time²³ by using bucket sorting algorithm while transversing the RAG.

Our framework uses the SRM algorithm, proposed by Nock and Nielsen,^{25,26} later adapted to deal with 3D images.³¹ As in other region classification algorithms, it aims at associating a pixel to a regions based upon a similarity criteria.^{6,12,16} Particular advantages of SRM are to rely on a simple interaction between a merging predicate and an order in merging in linear time.

An iterative process starts with one region per pixel, followed by merging phases after the calculation of a statistical test based on neighboring regions. This test considers an ascending order of intensity differences and checks if the mean intensities are sufficiently similar to be merged.³¹

The merging predicate, $P(R_i, R_j)$, decides whether the observed regions R_i and R_j belong to the same statistical region. The merging predicate assumes that the pixels from a statistical region have the same expectation, and it is represented as:

$$P(R_i, R_j) = \begin{cases} \text{true} & \text{if } |\bar{R}_i - \bar{R}_j| \leq b(R_i) + b(R_j) \\ \text{false} & \text{otherwise} \end{cases} \quad (3)$$

where the right-hand side of equation 3 is the center value between R_i and R_j , and it is used as a merging threshold. The variable b is a function of g , the largest possible intensity value (here, 255), S_l , the set of regions with l pixels, δ is the probability error¹⁵ and takes values in $0 \leq \delta \leq 1$. Q is the number of random variables, which somewhat translates the complexity of the scene and controls the coarseness of the segmentation, and $|\cdot|$ is the number of elements in the set of pixels.

$$b(R) = g \sqrt{\frac{1}{2Q|R|} \left(\frac{\ln|S_{|R|}|}{\delta} \right)} \quad (4)$$

In,²⁵ the probability acting on a pixel is replaced by the moving average over a neighborhood for handling image noise corruption. Instead, we used bilateral filtering to mitigate the noise and to preserve fluctuations related to borders. We use SRM algorithm such that its output contains regions, and each region, its average gray level. This representation serves as input to a new algorithm that determines two cut-offs based on the intensity histogram of the SRM combined with information extracted from the patches, previously selected by the user.

The proposed algorithm computes the relative difference (δ) between the average gray value of a foreground (μ_f) and a background (μ_b) patch and use it as part of a scheme to estimate suitable cut-offs to the result of SRM. This is possible due to the difference between the foreground (f) and background (b) patches, in terms of their mean, median, mode, maximum, minimum and intensity density, to be approximately constant. We use this realization as part of an optimization routine to determine two cut-offs that support the decision to split voxels into material and pore space. The optimization involves the search of two parameters \bar{p}_b and \bar{p}_f that maximize the number of voxels in f and b sets, constrained to fall within a range determined by the standard deviations (σ_b, σ_f), calculated from the training patches, and δ . The algorithm assumes the background is “dark” or “bright” based on the average level of the patches, then it initializes g_b and g_f . For example, the background is the dark portion if $\mu_b < \mu_f$. The scheme sets g_b to the minimum value of the SRM result and $g_f = g_b + \delta$, before it computes the sum of voxels centered p_b and p_f , iterating for increasing values of g_b and g_f . Given the substack histogram h , we define our problem as the maximization of the function $F(g_b, g_f)$, formally defined as follows:

$$\begin{aligned} & \underset{g_b, g_f}{\operatorname{argmax}} F(g_b, g_f) : |g_b - g_f| = \delta \\ F(g_b, g_f) = & \sum_{p_b = g_b - \sigma_b}^{g_b + \sigma_b} h(p_b) * k_b(p_b) + \sum_{p_f = g_f - \sigma_f}^{g_f + \sigma_f} h(p_f) * k_f(p_f) \end{aligned}$$

In order to decrease the contribution of non-center values of h , we compute the weighted average using a Gaussian kernel k , defined in the same interval of h . Despite the assumption of constant relative difference between μ_b and μ_f , the scheme performs well because of the quasi-homogeneous distribution of background and

foreground portions across the whole volume. This scheme could be generalized to deal with datasets where there may be monophasic subvolumes by adding a condition that considers a minimum volume of each phase before accepting g_b and g_f .

3. EXPERIMENTAL RESULTS

We evaluate the performance of the proposed framework by running two experiments, both involving comparison between the bilateral filtering and the iterative median filtering. The first experiment uses a synthetic image corrupted by different levels of Gaussian noise, using the assumption proposed in Heide et al¹⁸ that the micro-CT artifacts are normally distributed. The second experiment illustrates the result of filtering and segmenting a real micro-CT image, followed by comparison with a manual segmentation.

3.1 Application to synthetic data

We simulate 3D images to clearly illustrate the comparison between *med3* and bilateral filtering algorithms, using the same kernel size in both approaches. This study is based on previous researches dealing with tridimensional tomographic data and synthetic data.^{18,34} We used the same parameters for the bilateral filtering as in

Fig.4(a) illustrates a synthetic volume that emulates the cylinder that encloses the porous medium samples in real experiments. The cylinder voxels assume two values: 255 (17% of the voxels) and 0 (83% of voxels). Assuming that the micro-CT images present lowered signal-to-noise ratio due to data corruption, and it can be modeled as proposed, we simulate the image filtering/segmentation scheme applied to the synthetic data under different levels of additive Gaussian noise. In this study, the segmentation consists in applying a threshold ($T=128$) to separate the cylinder from the background. We demonstrate the performance of the iterative median filtering and bilateral filtering for different noise levels ($\sigma=[40:2:120]$). Particularly, Fig.4(b) shows the volume corrupted by Gaussian noise with standard deviation ($\sigma=75$). The *med3* filter is not accurate at the borders of the stack, an effect that accounts for most of the unidentified pixels for $\sigma < 80$. The bilateral filter recovers the original cylinder for $\sigma < 80$, and *med3* outperforms bilateral filter for higher σ values.

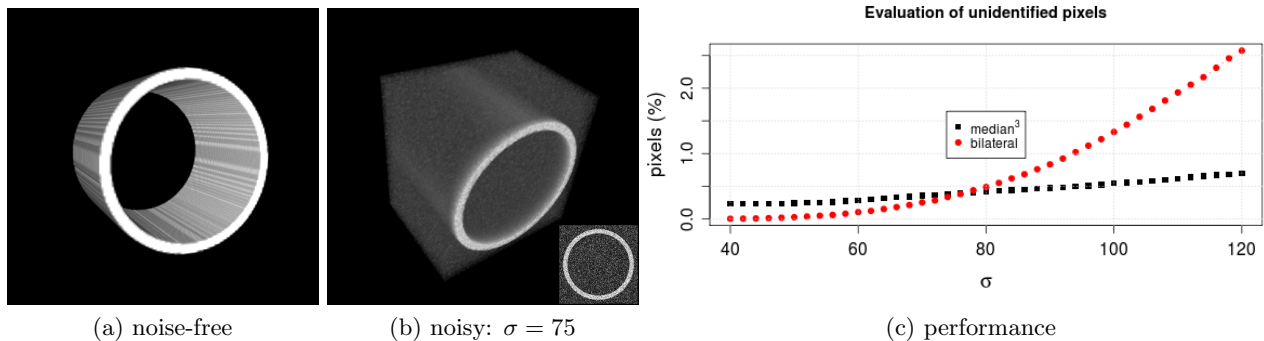


Figure 4: Analysis of segmentation for different levels of Gaussian noise: (a) synthetic image with 200x200x150 pixels (b) synthetic image corrupted with additive Gaussian noise with $\sigma = 75$ (c) analysis of segmentation performance for different levels of Gaussian noise using two denoising methods in terms of misclassified pixels: 3D iterative median filtering and 3D bilateral filtering ($\sigma_d = 3, \sigma_r = 200$).

3.2 Application to a rock from experimental data

The Gaussian assumption is often considered, however different noise models could be applied, e.g. Poisson distribution.³⁶ Without assuming a noise model, we perform noise-reduction using both *med3* and bilateral filtering, followed by thresholding and SRM segmentation. This comparison uses a manually segmented volume ($655 \times 440 \times 17 \mu\text{m}^3$) from Fig.5. We evaluate the performance between the techniques using two measures: (a) the sensitivity, which indicates the true positive (rock) fraction of the pixels and (b) specificity, the true negative (void) fraction of the pixels, calculated between the manually segmented image and the result of segmentation

Table 2: Evaluation of the methods for manually segmented rock.

Method	Sensitivity	Specificity	Time(s)
Bilateral+thresholding	0.87	0.92	0.7
Med3+thresholding	0.67	0.94	2.6
Bilateral+SRM	0.97	0.97	1.2
Med3+SRM	0.77	0.99	3.3

methods: thresholding and statistical region merging using either bilateral or *med3* filtering. The results of this comparison are summarized in Table 2.

According to these results, we notice that bilateral filtering is more sensitive than *med3* for both segmentation methods, while *med3* is slightly more specific. This is an useful way of gaining insight into the underlying behavior of the methods, and motivates our choice of inclusion of bilateral filtering into our pipeline, particularly regarding its computational time.

3.3 Results of proposed framework

We filtered and segmented the micro-CT stacks illustrated in Fig.5-8, at their full resolution, full-stack, 2^8 pixel depth and no grid coarsening, using the framework in Fig.1. At left of each figure, we show a slice of the geological sample before any processing and, at right, red lines indicate the result of the solid phase detection.

Fig.5(b) shows the result of segmentation from a geological sample, correctly detecting large grains, with partial inclusion of glass fibers, represented as fine grain bright spots at the periphery of the sample. Fig.6(b) illustrates the detection of solid material, corresponding to glass-beads and calcite precipitation, with partial exclusion of isolated calcite precipitation spots. Both Fig.7 and Fig.8 illustrates the result of separating the solid material, composed by small, fine grain structures from the rest of volume. The segmentation results of Fig.8 are mainly corrupted by the existence of a very heterogeneous definition of foreground, composed by 4 different phases.

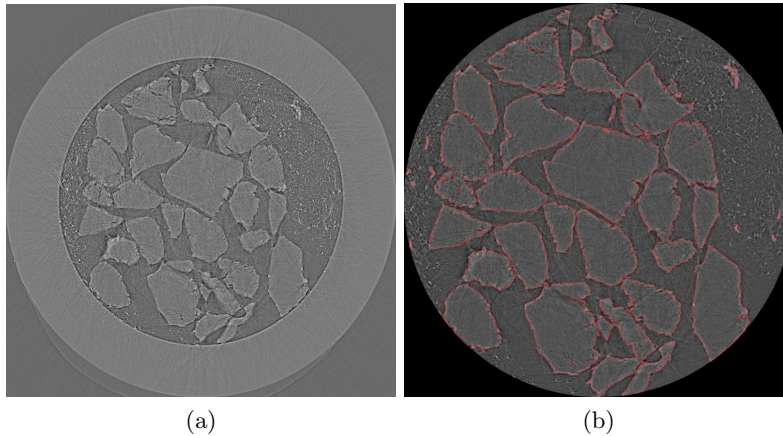


Figure 5: Iron oxide coated quartz sand composite for bioremediation experiments: (a) source data slice and (b) segmentation result, with red contours enclosing the solid phase of image (a).

Porosity is the amount of pore space in a rock, and we associate pore space to our estimated void volume. After separating the solid from the void volume, we calculate the porosity $\phi = V_v/V_t$, the quotient between the volume of void space (V_v) and the total volume (V_t), which includes the solid and void components. Table 3 shows measured porosity for each stack.

Fig.9 illustrates our best segmentation result using the stack in Fig.5 by showing a 3D volume rendering using VisIt, a high performance computing visualization tool with the ability to reconstruct material interfaces. This representation is often useful because it reveals pore connectivity across the sample, which is obscure when visualizing the 2D slices only.

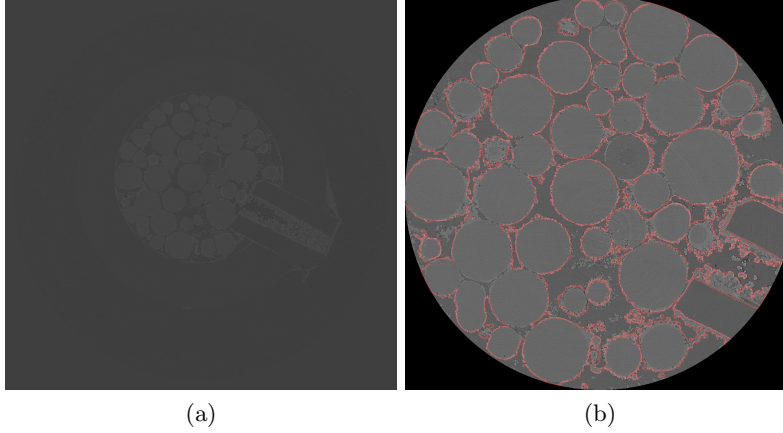


Figure 6: Composite and calcite formation: (a) source data slice and (b) segmentation result.

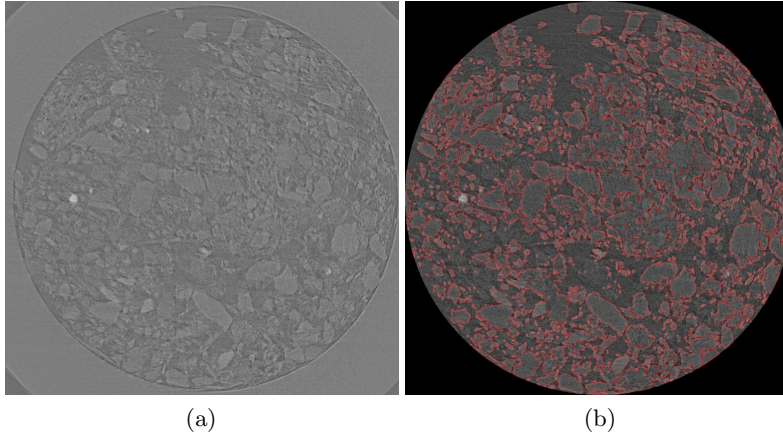


Figure 7: (Top) Column slice with small sediment grains used in bioremediation experiments: (a) source data slice and (b) segmentation of pore space, with performance deterioration due to high noise and scale of sediments.

Computations used National Energy Research Scientific Computing Center (NERSC)⁵ facility, particularly the machines Euclid, a Sun Microsystems Sunfire x4640 SMP, for running Fiji.³ Its single node contains eight 6 core Opteron 2.6 GHz processors with all 48 cores sharing the same 512 gigabytes of memory. Our code explores the large shared-memory to deal with embarrassingly parallel processing of substacks, an advantage of using Euclid over standard PCs. Volume rendering using VisIt⁴ took place at Franklin, the NERSC Cray XT4 system, a massively parallel processing system with 9,572 compute nodes. The framework includes filtering and segmentation of stacks and it was designed by combining, original and existent, macros and plugins, in Fiji,³ and can be run in any computer platform. All the processing and analysis can be centralized in a single platform (Euclid), when disregarding the visualization of full stacks.

Table 3: Results of porosity quantification for micro-CT volumes.

Figure	experiment	V_s (pel)	ϕ
5	large sediments	356,462,263	0.53
6	calcite	422,742,342	0.43
7	small sediments	443,333,272	0.33
8	several sediments	977,229,086	0.23

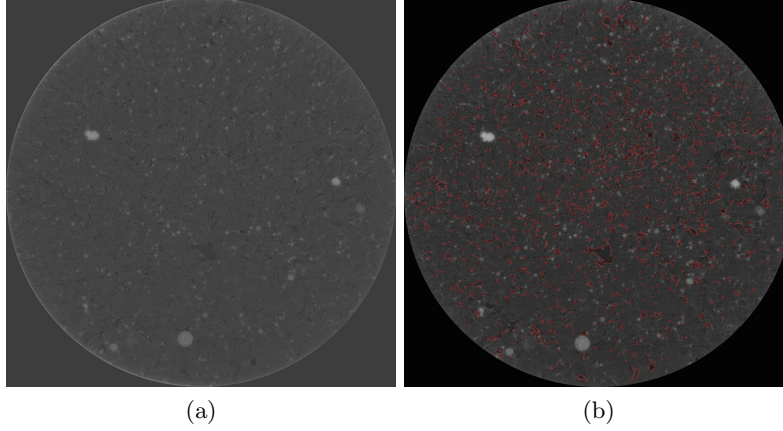
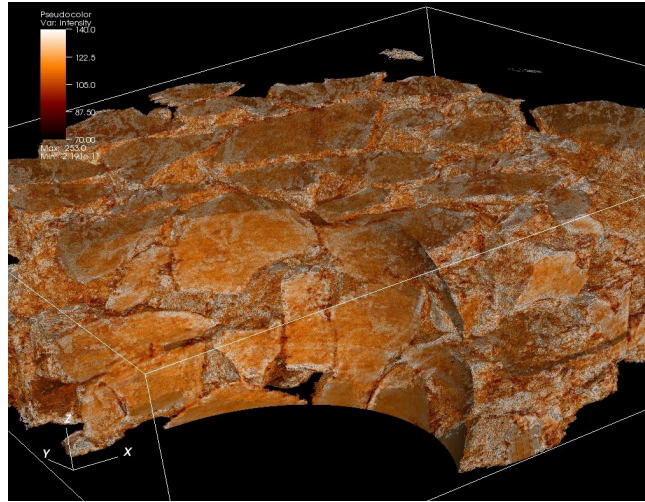


Figure 8: Shale type rock with 5 different phases: illite (medium to light gray) pore (dark gray) and pyrite (brightest spots): (a) source data slice and (b) segmentation of pore space.



(a)
Figure 9: VisIt volume rendering of Fig.5 and spherical slicing.

4. CONCLUSIONS AND DISCUSSION

We reported some of our latest results toward producing user-friendly software code that can address segmentation and porosity calculation of micro-CT 3D digital data sets. These results aim at benefiting fluid flow, transport and reaction modeling as an aid to answering problems in topics such as geologic CO₂ sequestration, magma effusiveness, groundwater plume contamination, water transport in plants. Most of the available codes for segmentation are customized to a specific dataset - we presented a computational scheme that we expect to handle different and heterogeneous datasets, as those tested and described in our paper.

Both synthetic and experimental data were carried out in testing different approaches for filtering and segmentation. Sec.3.1 showed that the *med3* outperformed bilateral for higher levels of Gaussian noise, otherwise bilateral was more accurate in recovering the synthetic 3D volume. Although the additive Gaussian noise model is a good approximation and widely considered, it does not account for artifacts that follows patterns as ring-like artifacts. In addition, Sec. 3.2 illustrated results of using manual segmentation as ground truth to evaluate the performance of different computational schemes for filtering and segmenting micro-CT and noticed that the proposed scheme, using 3D bilateral filtering and 3D SRM, correctly detected more voxels than other approaches. Finally, Sec.3.3 showed the results of using such a scheme applied to a variety of micro-CT datasets. The average amount of time to filter and segment a micro-CT slice from our dataset is about 5 seconds.

Our results are based on standard implementations of the filters that requires $O(d^k)$ per pixel, with kernel size ($k = 3$) fixed at a diameter (d) of 3 pixels. Since the computational complexity is related to the third power of the diameter, the bilateral filter geometric parameter was kept constant at $k = 3$. Using Java implementations for Fiji,³ we measured that the bilateral filter was approximately 3 times faster than *med3*, according to evaluation of our synthetic and real data. Other implementations of bilateral filtering includes discretization of image intensities and adaptation of block size, which can improve time complexity to $O(1)$.³⁶ Alternative optimized implementations regard linear separability of Gaussian kernels,²⁹ approximation by using signal processing²⁸ and adaptive methods that includes statistical noise models (e.g. Poisson distribution).³⁵ As for the median filtering, if one considers the quick select algorithm, it can lead to the best-case $\Omega(n \log n)$ time, where n is the length of the list, given the fact that the sorting of all pixel values is not necessary.¹⁸

One of our contributions is to propose a framework that estimates suitable parameters for image filters automatically, using samples selected by the user. This scheme works by adjusting the photometric parameter (intensity variation), which ultimately, define the weights to the kernel function to be convolved with the image. We use the statistical region merging algorithm to differentiate sets of pixels with similar intensities, considering adjacency in the merging process - this outputs the average gray levels representing each detected region. We propose a method to split the SRM output into solid and pore space, using statistics of patches selected in the training phase. The segmentation result was input to porosity quantification, which we calculated using the fraction between the detected materials and the void space from geological samples.

While we mostly circumvent brightness variation across the sample and sensitivity to small sediments, dealing with multiphase materials is still a limitation of our approach. Although we considered manual segmentation to evaluate the proposed approach, further comparisons using known porosity materials and respective automated segmentation results are to be delivered. Future work might consider optimized implementations of the bilateral filtering and statistical regions merging, including extension to multiphase porous media. We intend to improve the characterization of the material structure, by representing connectivity of pores in channel structures, as illustrated in our preliminary work using Reeb graphs in.³³ Further feature extraction could include branch-node network to describe channeling, which may allow prediction of transport through the porous network of the material.

5. ACKNOWLEDGEMENTS

This work was mostly supported by the Director, Office of Science, Office of Basic Energy Sciences and Office of Advanced Scientific Computing Research, of the U.S. Department of Energy under Contract No. DE-AC02-05CH11231 through the Scientific Discovery through Advanced Computing (SciDAC) programs Visualization and Analytics Center for Enabling Technologies (VACET). Also, it was partially supported by the Applied Mathematical Science subprogram of the Office of Energy Research, U.S. Department of Energy, under Contract Number DE-AC03-76SF00098.

REFERENCES

- [1] Advanced Light Source (ALS), <http://www-als.lbl.gov/>
- [2] Energy Frontier Research Center (EFRC), <http://esd.lbl.gov/research/facilities/cncgc/>
- [3] Fiji, <http://pacific.mpi-cbg.de/wiki/index.php/Fiji>
- [4] Visit, <http://www.visit.llnl.org>
- [5] National Energy Research Scientific Computing Center (NERSC), <http://www.nersc.org>
- [6] Alattar, M.A., Osman, N.F., Fahmy, A.S.: Myocardial segmentation using constrained multi-seeded region growing. In: International Conference on Image Analysis and Recognition (ICIAR10). pp. II: 89–98. LNCS (2010)
- [7] Armstrong, R., Ajo-Franklin, J.: Investigating biomineralization using synchrotron based x-ray computed microtomography. *Geophys. Res. Lett.* 38 (2011)
- [8] Bethel, E.W.: High Performance, Three-Dimensional Bilateral Filtering. Tech. Rep. LBNL-1601E, Lawrence Berkeley National Laboratory, Berkeley, CA, USA, 94720 (2009)

- [9] Brasse, D., Humbert, B., Mathelin, C., Rio, M.C., Guyonnet, J.L.: Towards an inline reconstruction architecture for micro-ct systems. *Phys.Med.Biol.* 50, 5799–5811 (2005)
- [10] Brun, F., Kourousias, G., Dreossi, D., Mancini, L.: An improved method for ring artifacts removing in reconstructed tomographic images. In: Magjarevic, R., Dssel, O., Schlegel, W.C. (eds.) *World Congress on Medical Physics and Biomedical Engineering*, September 7 - 12, 2009, Munich, Germany, IFMBE Proceedings, vol. 25/4, pp. 926–929. Springer Berlin Heidelberg (2010)
- [11] Buades, A., Coll, B., Morel, J.M.: Image denoising methods. a new nonlocal principle. *SIAM Review* 52(1), 113–147 (2010)
- [12] Carvalho, E., Ushizima, D., Medeiros, F., Martins, C., Marques, R., Oliveira, I.: Sar imagery segmentation by statistical region growing and hierarchical merging. *Digital Signal Processing* 20(5), 1365–1378 (2010)
- [13] Dierick, M., Masschaele, B., Hoorebeke, L.V.: Octopus, a fast and user-friendly tomographic reconstruction package developed in labview. *Meas. Sci. Technol.* 15(7), 1366 (2004)
- [14] Elliot, T., Heck, R.: A comparison of 2d vs. 3d thresholding of x-ray ct imagery. *Can. J. Soil Sci.* 87, 405412 (2007)
- [15] Fahad, A., Morris, T.: A faster graph-based segmentation algorithm with statistical region merge. In: Bebis, G., Boyle, R., Parvin, B., Koracin, D., Remagnino, P., Nefian, A., Meenakshisundaram, G., Pascucci, V., Zara, J., Molineros, J., Theisel, H., Malzbender, T. (eds.) *Advances in Visual Computing, Lecture Notes in Computer Science*, vol. 4292, pp. 286–293. Springer Berlin / Heidelberg (2006)
- [16] Gonzalez, R.C., Woods, R.E.: *Digital Image Processing (3rd Edition)*. Prentice-Hall, Inc., Upper Saddle River, NJ, USA (2006)
- [17] Hamarneh, G., Hradsky, J.: Bilateral filtering of diffusion tensor mr images. *International Symposium on Signal Processing and Information Technology* 0, 507–512 (2006)
- [18] van der Heide, P., Xu, X.P., Marsh, B.J., Hanein, D., Volkmann, N.: Efficient automatic noise reduction of electron tomographic reconstruction based on iterative median filtering. *Journal of Structural Biology* 158, 196–204 (2007)
- [19] Kak, A.C., Slaney, M.: *Principles of Computerized Tomographic Imaging*. Society of Industrial and Applied Mathematics (2001)
- [20] Keiner, J., Kunis, S., Potts, D.: Using nfft 3 - a software library for various nonequispaced fast fourier transforms. *ACM Trans. Math. Softw.* 36, 19:1–19:30 (August 2009)
- [21] Kinney, J., Nichols, M.: X-ray tomographic microscopy using synchrotron radiation. *Annu. Rev. Mater. Sci.* pp. 22–121 (1992)
- [22] Lux, J., Delisee, C., Thibault, X.: 3d characterization of wood based fibrous materials: an application. *Image Anal. Stereol.* 25, 25–35 (2005)
- [23] McGuinness, K., Keenan, G., Adamek, T., O'Connor, N.E.: Image segmentation evaluation using an integrated framework. In: *4th International Conference on Visual Information Engineering. IET'07*, London, UK (2007)
- [24] Nico, P.S., Ajo-Franklin, J.B., McDowell, A., Silin, D.B., Tomutsa, L., Benson, S.M., Wu, Y.: Synchrotron x-ray micro- tomography and geological co2 sequestration. *Advances in Computed Tomography for Geomaterials - GeoX 2010* pp. 374–380 (2010)
- [25] Nock, R., Nielsen, F.: Statistical region merging. *IEEE Transactions on Pattern Analysis and Machine Intelligence* 26, 1452–1458 (2004)
- [26] Nock, R., Nielsen, F.: Semi-supervised statistical region refinement for color image segmentation. *Pattern Recognition* 38, 835–846 (2005)
- [27] Oh, W., Lindquist, W.B.: Image thresholding by indicator kriging. *IEEE Trans PAMI* 21, 590–602 (1999)
- [28] Paris, S., Durand, F.: A fast approximation of the bilateral filter using a signal processing approach. *Int. J. Comput. Vision* 81, 24–52 (January 2009)
- [29] Pham, T.Q., Vliet, L.J.: Separable bilateral filtering for fast video preprocessing. In: *IEEE Internat. Conf. on Multimedia Expo, CD14*. pp. 1–4. IEEE (2005)
- [30] Porter, M., Wildenschild, D.: Image analysis algorithms for estimating porous media multiphase flow variables from computed microtomography data: a validation study. *Comput Geosci* 14, 1530 (2009)

- [31] Schindelin, J.: Statistical region merging (2009), http://pacific.mpi-cbg.de/wiki/index.php/Statistical_Region_Merging#cite_note-0
- [32] Tomasi, C., Manduchi, R.: Bilateral filtering for gray and color images. In: Proceedings of the Sixth International Conference on Computer Vision. pp. 839–. ICCV '98, IEEE Computer Society, Washington, DC, USA (1998)
- [33] Ushizima, D., Weber, G., Ajo-Franklin, J., Kim, Y., Macdowell, A., Morozov, D., Nico, P., Parkinson, D., Trebotich, D., Wan, J., Bethel, W.: Analysis and visualization for multiscale control of geologic CO₂. Scientific Discovery through Advanced Computing (Scidac'2011) (2011)
- [34] Wang, W., Kravchenko, A., Smucker, A., Rivers, M.: Comparison of image segmentation methods in simulated 2d and 3d microtomographic images of soil aggregates. *Geoderma* 162, 231–241 (2011)
- [35] Yu, L., Manduca, A., Jacobsen, M., Trzasko, J.D., Fletcher, J.G., DeLone, D.R., McCollough, C.H.: Adaptive modulation of bilateral filtering based on a practical noise model for streaking and noise reduction in multi-slice ct. *Proc. SPIE on Medical Imaging* pp. 1–7 (2010)
- [36] Yu, W., Franchetti, F., Hoe, J.C., Chang, Y.J., Chen, T.: Fast bilateral filtering by adapting block size. In: 17th International Conference on Image Processing. ICIP'10, Hong Kong (2010)
- [37] Zandomeneghi, D., Voltolini, M., Mancini, L., Brun, F., Dreossi, D., Polacci, M.: Quantitative analysis of x-ray microtomography images of geomaterials: Application to volcanic rocks. *Geosphere* 6(6), 793–804 (2010)